Excitation of Initial Waves by Wind: A Theoretical Model and Its Experimental Verification

Meital Geva● and Lev Shemer●*

School of Mechanical Engineering, Tel-Aviv University, Tel Aviv 6997801, Israel

We present a theory of evolution of wind waves in time and space under abruptly applied wind forcing that is experimentally validated in a laboratory wind-wave tank. The model describes qualitatively and quantitatively the complex wave field development from the initial smooth surface to the finite state. The stochastic nature of wind waves is treated by considering an ensemble of coexisting unstable harmonics that grow due to shear flow instability. Breaking limits the wave growth initially; the process is then controlled by fetch-limited growth duration.

It has been realized since ancient times that sea waves are caused by wind, yet mechanisms leading to development of young waves are not fully understood. In nature, wind varies in time and in space, whereas the existing theories mostly consider impulsively applied steady airflow; spatial homogeneity of the wave field is assumed at each instant. Two distinct physical mechanisms leading to wind-wave excitation have been proposed. The shear flow instability theory initiated by Miles [1] stresses the importance of the so-called critical layer at the elevation above the mean water surface where the wave phase velocity equals the mean wind velocity. This linear, deterministic, and unidirectional approach was further developed in numerous studies [2–6]. It predicts exponential growth in time of multiple harmonics, although the analysis was mainly focused on the most unstable wave. An alternative mechanism suggested by Phillips [7] relates the growth of water waves to nonresonant and resonant interactions between the waves and the pressure fluctuations in the turbulent airflow over the water surface. His model is random and nonlinear; it takes into account the directional spreading of nonlinear wind waves and predicts linear wave energy increase with time in two stages. The Miles model and its developments attained greater attention, in part since the verification of the Phillips theory requires estimates of air pressure fluctuations; this task poses nearly insurmountable difficulties [8]. Numerous studies [9–12] dealt with the effect of turbulent airflow over a moving deterministic wavy surface on wind-wave growth.

No theoretical description of the waves' evolution from initially quiescent water surface to finite steady state is currently available [13]. Evidence of existence of a critical layer in field experiments provided an indirect support for the Miles theory [14,15]. Initial exponential growth of energy of short waves excited by impulsively applied wind on quiescent water surface was reported in [3]. These results are in qualitative agreement with the growth of the most unstable mode predicted by viscous shear-flow instability at the air-water interface that is governed by the coupled Orr-Sommerfeld equations [2,3]. Recently, results of direct numerical simulations [16] indicated that initial stages of wind-wave growth may be compatible with the Phillips [7] model. Radar measurements in a wind-wave tank subjected to a suddenly applied wind demonstrated not just a single but rather multiple exponentially growing harmonics coexist in the wave field [17]. Later experiments indicated that the minimum friction velocity u_* required for excitation of wind waves is consistent with the predictions of shear-flow instability theory [18]. It is argued, however, that wind-wave evolution is mainly governed by nonlinear wave-wave interactions, while details of parametrization of wind input and wave energy dissipation are less important [19,20].

The approaches in [1,7] assume temporal growth of the spatially homogeneous wind-wave field under impulsive wind forcing, whereas in most experiments, steady wind forcing is applied. The variation of the amplitude and the wavelength of wind waves is studied as a function of the distance from the inlet x (fetch) [21,22]. Qualitative agreement with experiments was obtained in simulations of the spatial evolution of waves using phenomenological expressions for wind input and wave dissipation [23]. Accounting for nonlinear interactions among waves using the spatial Zakharov equation [24,25] improved the agreement between simulations and measurements, although the numerical predictions still differ from the experimental results. So far, no model exists that enables description of combined spatial and temporal wave field evolution. Here we offer a novel theoretical approach that describes such evolution of waves under impulsive wind forcing.

The present Letter is aimed at providing a physical insight into the multistage waves evolution documented in our wind-wave facility [26]. In those experiments, wind-wave parameters were recorded as a function of time t

evolved since wind initiation, at several fetches x and wind velocities U_0. The accumulated data demonstrate that wind waves are random and lose coherence fast [8]. In each experimental run, the measured instantaneous surface elevation $\eta(t)$ thus represents superposition of independent harmonics with random phases. Multiple runs performed for each value of U_0 allowed obtaining reliable ensemble-averaged time-dependent characteristic wave amplitudes $\langle\eta^2\rangle^{1/2}$ and the instantaneous dominant frequencies f_{dom} obtained using the wavelet analysis [26]. In these experiments, the representative ensemble-averaged surface slope component $\langle(\partial\eta/\partial x)^2\rangle^{1/2}$ was also recorded. The technical details of experiments performed in [26] are summarized in the Supplemental Material [27]. The complex pattern of variation in time of the parameters plotted in Fig. 1 is common for different fetches and wind velocities U_0. In all cases, the growth of the surface slope that represents the wave steepness precedes that of the surface elevation amplitude and attains quasisteady state notably earlier than $\langle\eta^2\rangle^{1/2}$. The decrease in f_{dom} indicates that the dominant wave length increases with t. Figures 1(b) and 1(c) show that the wave field is characterized by random waves with multiple length scales and directions. The initial waves are spatially homogeneous, while inhomogeneity emerges

later, so that longer waves are only observed at larger fetches [8]. The random wave nature is treated using the ensemble-averaged quantities plotted in Fig. 1(a).

Figure 1 demonstrates that $\langle\eta^2(t)\rangle^{1/2}$ seems to grow exponentially initially, but this stage terminates fast and is followed by a much slower growth at a varying rate. Based on this observation, disturbances on an initially smooth water surface triggered by turbulent airflow fluctuations are assumed to grow exponentially; this suggests that the process can be described by a linear model. It is further assumed that during the early stages of evolution, the wave field is spatially homogeneous and can be seen as a superposition of independent unidirectional harmonics characterized by their wave numbers k_i, radian frequencies ω_i, and random phases. The stability of each harmonic and its corresponding energy growth rate $\beta(k_i)$ are governed by viscous shear-flow instability at the air-water interface. This instability is described by the coupled Orr-Sommerfeld (OS) equations [2,3] written in terms of stream functions in air and in water for two-dimensional spatially homogeneous incompressible flow. The OS model requires mean velocity profiles $U(z)$ in air and in water as input. Turbulence in airflow is accounted for using the lin-log profile over smooth water surface suggested by Miles [28]. This profile consists of a linear segment in the viscous sublayer smoothly connected to the logarithmic part; it was applied in previous wind-wave generation studies [2,3,5,6]. In water, the velocity decays exponentially with depth from the surface drift velocity U_d [3,6]. Both velocity profiles are defined by the air friction velocity at air-water interface, $u_* = (\tau/\rho)^{1/2}$, where τ is the interfacial shear stress and ρ is the air density. Experimental evidence suggests that for $U_0 = $ const., u_* does not vary notably along the whole test section [29–31]. For detailed presentation of the OS equations, boundary conditions, adopted velocity profiles, and the general description of the computational procedure and its validation see the Supplemental Material [27].

The solution of the coupled OS equations for a wave number k_i yields a complex eigenvalue $\omega_i(k_i) = \omega_{i,R}(k_i) + i\omega_{i,I}(k_i)$; here the real and the imaginary parts of ω_i represent the angular wave frequency and wave amplitude
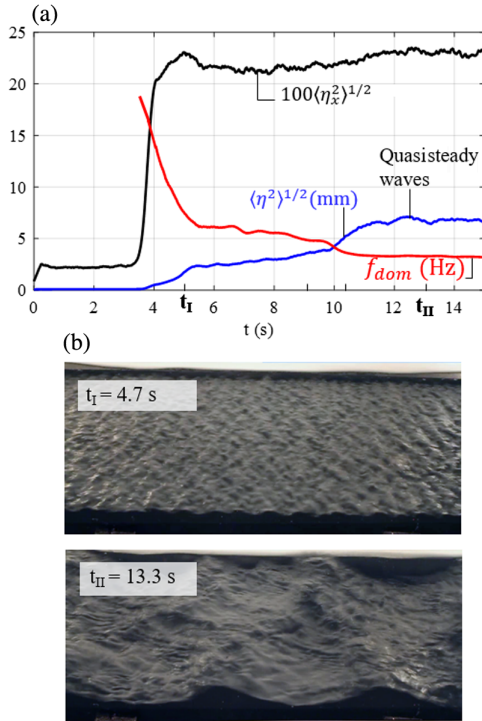

FIG. 1. Wind waves under wind forcing at $U_0 = 10.5$ m/s ($u_* = 0.65$ m/s) and $x = 260$ cm: (a) evolution as a function of time elapsed from the blower initiation of the ensemble-averaged surface elevation $\langle\eta^2\rangle^{1/2}$, slope $\langle(\partial\eta/\partial x)^2\rangle^{1/2}$, and the dominant frequency f_{dom}; (b) snapshots of the surface elevation at 256 cm < x < 288 cm selected from a video record synchronized with the initiation of the blower. Wind blows from right to left.
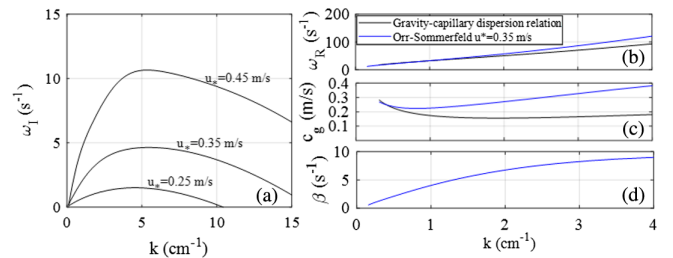

FIG. 2. Results of the coupled OS solver. (a) Amplitude growth rate vs wave number k_i estimated at various u_*. (b)–(d) Solutions for $u_* = 0.35$ m/s (blue line) vs gravity-capillary dispersion relation (black line); (b) dispersion relation $\omega_R(k)$; (c) group velocity $c_g(k)$; (d) energy growth rate $\beta(k)$.

growth rate, respectively. Figure 2(a) defines the domains of instability where $\omega_I > 0$ for selected values of u_*. Increase in u_* results in extension of the range of unstable wave numbers and larger maximum growth rates. To carry out validation with experiments, the moderate value of $u_* = 0.35$ m/s was selected. For this u_*, the forcing is effectively impulsive [26]. Figure 2(b) demonstrates that the computed dependence $\omega_R(k)$ and the linear dispersion relation for gravity-capillary waves in the absence of wind collapse on a single curve for longer waves. The wave energy of each spectral harmonic propagates along the test section with its group velocity $c_g = d\omega_R/dk$ that is presented in Fig. 2(c). For larger values of k, the OS-derived values of c_g and ω_R exceed those of gravity-capillary waves. This is attributed to the Doppler shift caused by the wind-induced current. The OS-derived results in Figs. 2(b) and 2(c) compare well with the experimentally determined dispersion relation [22,32]. The exponentially growing energy of each harmonic

$$E_i = E_{i,0} \exp\left(\beta_i t\right) \tag{1}$$

is related to its squared amplitude $a_i'^2(t)$; the energy growth rates $\beta(k) = 2\omega_I(k)$ are plotted in Fig. 2(d) and decrease notably with wave length $\lambda = 2\pi/k$.

This deterministic analysis is now applied to a stochastic ensemble of temporally evolving coexisting unstable harmonics. The characteristic amplitudes of the surface elevation at each instant are estimated as the expected value of the stochastic system of all unstable harmonics. Each harmonic is assumed to have identical likelihood, equal initial amplitudes $a_i'(t = 0)$ and random phase. The average of all possible outcomes of N measurements weighted by their likelihood is interpreted as the expected value for a large ensemble of independent realizations [33]

$$\langle \eta^2(t) \rangle^{1/2} = \sqrt{\sum \frac{a_i'^2(t)}{N}}. \tag{2}$$

Note that, since the spectral amplitudes a_i satisfy the relation

$$\langle \eta^2(t) \rangle^{1/2} = \sqrt{\sum a_i^2(t)}, \tag{3}$$

it is evident from comparison of Eqs. (2) and (3) that $a_i'(t) = a_i(t) \cdot \sqrt{N}$; they both grow at the rate $\beta_i/2$ [Fig. 2(d)]. The experimental equivalent of the expected value of the surface elevation corresponds to ensemble averaging of the instantaneous surface elevations measured in multiple runs. It should be stressed that, in unsteady experiments, the individual harmonics cannot be identified.

Since harmonics in different runs have random phases, in the stochastic ensemble of independent runs $\langle E_i(t) \rangle$ is related to the amplitude a_i' of each harmonic as $\langle E_i(t) \rangle = \langle a_i'^2(t) \rangle/2$. The expected surface elevation given by Eq. (3)
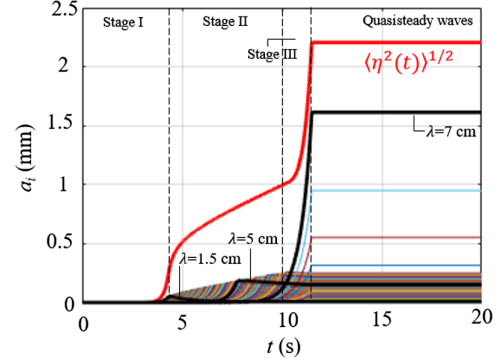

FIG. 3. Amplitudes' variation at $u_* = 0.35$ m/s, $x = 260$ cm of $N = 150$ equally spaced harmonics, $2\pi/30\,\mathrm{cm}^{-1} < k_i < 2\pi/1.5\,\mathrm{cm}^{-1}$ [27]. Evolution of selected wavelengths is plotted by bold black lines; the instantaneous expected surface elevation is plotted in red. The initial amplitudes in simulations correspond to $\langle \eta^2(0) \rangle^{1/2} = 1.6 \times 10^{-7}$ mm that defines the instant of appearance of the initial detectable disturbances since the initiation of the wind. The time increment $\Delta t = 0.05$ s.

is plotted in Fig. 3 alongside the temporal evolution of all harmonics considered in the simulations. Following [34], we assume that the maximum slope of each harmonic $s_{\mathrm{max},i}$ at the initial growth stage is restricted by breaking due to nonlinearity. In Fig. 3, we take $s_{\mathrm{max}} = k_i \cdot \langle E_i(t) \rangle^{1/2} = 0.2$, in agreement with [34] and compatible with the maximum slope measurements at this wind velocity [9,26,35]. This limit is somewhat lower than the maximum possible steepness of a monochromatic wave predicted by Stokes as observed in numerous experiments [36,37].

The steepness limit is attained earlier for faster growing shorter harmonics with large k_i [see Fig. 2(d)], while longer waves continue to grow to larger amplitudes, until their growth stops upon attaining s_{max}. The bold black curves in Fig. 3 depict the temporal variation of three selected harmonics. The linear stage in the evolution (stage I) corresponds to the unrestricted exponential growth of all harmonics. This stage terminates once the shortest wave in the ensemble attains its maximum steepness. This instant corresponds to the inflection point in $\langle \eta(t)^2 \rangle^{1/2}$ and to the onset of stage II. The wave growth during stage II is associated with the exponential increase in energy of longer harmonics limited by their steepness. Upon attaining their maximum amplitudes, harmonics are sheltered by higher and longer waves. They stop growing and decay at the rate $-2\nu k_i^2$ [38], where ν is the water kinematic viscosity, as exemplified by bold lines in Fig. 3 for $\lambda = 1.5$ and $\lambda = 5$ cm that have a sharp change in slope at $t = 4.3$ and $t = 7.8$ s, respectively. The decay of longer waves is notably slower. This sheltering mechanism is considered theoretically in [10] and verified experimentally in [9,39]. It is demonstrated in those studies that momentum and energy exchange between airflow and waves does not occur at length scales shorter than that of the dominant wave.

Nonlinearity introduced into this quasilinear model by accounting for sheltering by longer waves and for the limit on the maximum steepness of each harmonic thus leads to a visibly linear growth of the expected total wave energy $\langle \eta(t)^2 \rangle$, in agreement with Phillips [7] and with [16]. Note that during stage II, the wave field is still spatially homogeneous.

The termination of stage II is associated with the loss of homogeneity. In stage III, the wave field evolution is governed by the maximum possible duration $t_{\max,i}$ of the ith harmonic at a given fetch x. Since the energy propagates with the group velocity $c_{g,i}$, the wave excited at the inlet arrives at the measuring location x at

$$t_{\max,i} = x/c_{g,i}. \tag{4}$$

The maximum growth duration determined by Eq. (4) puts a limit on the growth of each harmonic. Fast, very short harmonics attain the limit earlier, see Fig. 2(c). The spatial homogeneity only holds for longer fetches x where the condition (4) is not yet attained. Once all harmonics reach this limit, steady state (stage IV) is attained at a given fetch x.

The suggested model is now compared with experiments performed at $u_* = 0.35$ m/s at three fetches [26]. The characteristic surface elevations $\langle \eta^2(t) \rangle^{1/2}$ measured at these locations are plotted in Fig. 4(a); the corresponding model-derived values are presented in Fig. 4(b). The evolution stages can be clearly identified in both panels. At each x, the simulations faithfully describe the transition times between the stages. The wave field homogeneity requires identical values of $\langle \eta^2(t) \rangle^{1/2}$ and of f_{dom} at all

fetches. The dependencies of $\langle \eta^2(t) \rangle^{1/2}$ at all fetches collapse on a single curve for about 5 s. The divergence of the curves in Figs. 4(a) and 4(b) manifests the loss of homogeneity; it occurs earlier for shorter x and thus smaller $t_{\max}$. The characteristic surface elevation in simulations and in experiments agree well during all stages of evolution. The instantaneous dominant frequency $f_{\mathrm{dom}}(t)$ estimated in the experiments by wavelet analysis is compared with the model-derived frequencies corresponding to the harmonic with the largest instantaneous amplitude, see Fig. 4(c). Both the measured and the computed values of f_{dom} compare favorably and decay fast from initially high value exceeding 15 Hz. Comparison of the measured and the simulated surface slopes is carried out in the Supplemental Material [27].

The whole complicated multistage process of evolution in time and space of the characteristic surface elevation amplitudes and of the dominant frequencies as measured in [26] can be accurately described by an essentially linear model amended by appropriate limits on the possible wave growth. Although it is generally assumed that the linear approach is limited to the initial stages in the evolution process, the present model remains valid well beyond the early evolution stages. The three-dimensional nature and lack of temporal and spatial coherence are accounted for reasonably well by the stochastic approach that contains all possible modes. Although the OS equations assume spatial homogeneity, the model describes adequately the fetch dependence observed in experiments at later stages of evolution. The initially homogeneous growth of the individual harmonics is limited by breaking; the finite propagation duration then renders the wave field inhomogeneous. Young wind waves may become quite steep; nevertheless, nonlinear wave-wave interactions apparently have only a secondary effect on the variation of the wave energy and of the dominant frequency in time and space. The evolution process is governed mainly by combination of viscous shear-flow instability and breaking of shorter harmonics, as well as their sheltering by longer and higher waves. Finite propagation duration governs the later evolution stage. Nonlinear interactions among young wind waves may constitute one of the reasons for some discrepancies between the experiments and simulations.

Additional successful experimental verification of the present model for stronger wind forcing with $u_* = 0.45$ m/s is given in the Supplemental Material [27]. Some quantitative discrepancy between the model and the experiments is found at the final stage of evolution. It should be stressed that the present OS computations assume an air velocity profile over a smooth water surface [3,6,28]. This assumption does not hold for higher wind velocities and larger fetches where the growing waves contribute to a significant surface roughness. The agreement between the simulations and experiments is still reasonable. The effect of roughness caused by wind waves on the OS-based stability analysis needs examination in
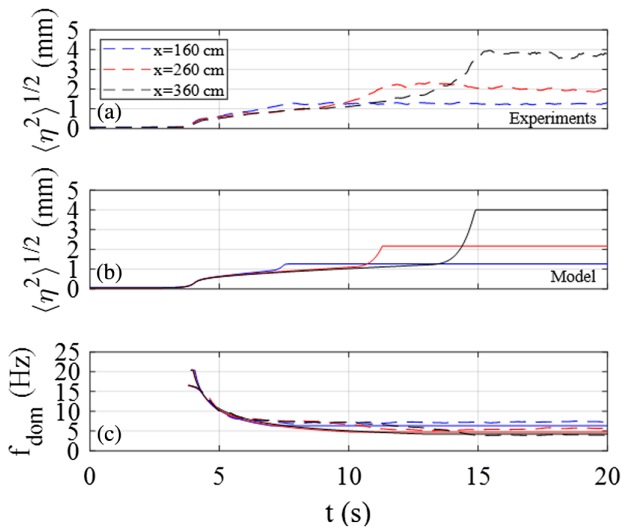

FIG. 4. Temporal evolution of wind waves at three fetches x at $u_* = 0.35$ m/s. (a) The measured characteristic wave amplitude. (b) The simulated characteristic wave amplitude. (c) The dominant frequency in simulations (solid lines) and experiments (broken lines).

future studies. An additional factor that prevents quantitative comparison of the model predictions with experiments at even higher wind velocities is related to the inevitable finite blower response time [26]. At higher blower settings, the forcing in the experiments cannot be seen as effectively impulsive. Nevertheless, the multistage pattern described by the present model is observed at various wind forcing conditions [26], up to a quite strong wind corresponding to $u_* = 0.65$ m/s, see Fig. 1(a).

In summary, understandings of the physical mechanisms governing excitation and growth of young wind waves under impulsive forcing gained in this study constitute a basis for quantitative modeling of wind-wave formation and growth in time and space under more general forcing conditions. The suggested framework can potentially be extended also to larger scales.

---

[*] shemerl@tauex.tau.ac.il

[1] J. W. Miles, J. Fluid Mech. **3**, 185 (1957).
[2] G. R. Valenzuela, J. Fluid Mech. **76**, 229 (1976).
[3] S. Kawai, J. Fluid Mech. **93**, 661 (1979).
[4] G. H. Wheless and G. T. Csanady, J. Fluid Mech. **248**, 363 (1993).
[5] W. T. Tsai and M. Y. Lin, J. Mar. Sci. Technol. **12**, 200 (2004).
[6] A. Zeisel, M. Stiassnie, and Y. Agnon, J. Fluid Mech. **597**, 343 (2008).
[7] O. M. Phillips, J. Fluid Mech. **2**, 417 (1957).
[8] L. Shemer, Atmosphere **10**, 562 (2019).
[9] M. P. Buckley, F. Veron, and K. Yousefi, J. Fluid Mech. **905**, A31 (2020).
[10] S. E. Belcher and J. C. R. Hunt, J. Fluid Mech. **251**, 109 (1993).
[11] M. A. C. Teixeira and S. E. Belcher, Dynam. Atmos. Oceans **41**, 1 (2006).
[12] V. K. Makin and V. N. Kudryavtsev, J. Geophys. Res. **104**, 7613 (1999).
[13] N. Pizzo, L. Deike, and A. Ayet, Phys. Today **74**, No. 11, 38 (2021).
[14] T. Hristov, S. Miller, and C. Frieh, Nature (London) **422**, 55 (2003).
[15] T. Hristov, C. Friehe, and S. Miller, Phys. Rev. Lett. **81**, 5245 (1998).
[16] T. Li and L. Shen, J. Fluid Mech. **934**, A41 (2022).
[17] T. R. Larson and J. W. Wright, J. Fluid Mech. **70**, 417 (1975).
[18] K. K. Kahma and M. A. Donelan, J. Fluid Mech. **192**, 339 (1988).
[19] V. E. Zakharov, S. I. Badulin, P. A. Hwang, and G. Caulliez, J. Fluid Mech. **780**, 503 (2015).
[20] V. E. Zakharov, S. I. Badulin, V. V. Geogjaev, and A. N. Pushkarev, Earth Space Sci. **6**, 540 (2019).
[21] W. G. Plant, J. Geophys. Res. Oceans **87**, 1961 (1982).
[22] A. Zavadsky and L. Shemer, Phys. Fluid **29**, 056602 (2017).
[23] L. Shemer and S. K. Singh, and A. Chernyshova, J. Fluid Mech. **901**, A22 (2020).
[24] V. E. Zakharov, J. Appl. Mech. Tech. Phys. **9**, 190 (1968).
[25] L. Shemer, K. Goulitski, and E. Kit, Eur. J. Mech. B Fluids **26**, 193 (2007).
[26] A. Zavadsky and L. Shemer, J. Fluid Mech. **828**, 459 (2017).
[27] See Supplemental Material at http://link.aps.org/supplemental/10.1103/PhysRevLett.128.124501 for technical details of the experiments, Orr-Sommerfeld solver, surface slopes, and additional experimental validation at $u_* = 0.45$ m/s.
[28] J. W. Miles, J. Aeronaut. Sci. **24**, 704 (1957).
[29] A. Zavadsky and L. Shemer, J. Geophys. Res. Oceans **117**, C00J19 (2012).
[30] W. J. Plant and J. W. Wright, J. Fluid Mech. **82**, 767 (1977).
[31] M. Geva and L. Shemer, J. Fluid Mech. **935**, A42 (2022).
[32] D. Liberzon and L. Shemer, J. Fluid Mech. **681**, 462 (2011).
[33] C. M. Grinstead and J. L. Snell, *Introduction to Probability* (American Mathematics Society, Rhode Island, 2012).
[34] M. S. Longuet-Higgins, Proc. R. Soc. A **435**, 405 (1991).
[35] F. Veron and W. K. Melville, J. Fluid Mech. **446**, 25 (2001).
[36] S. R. Massel, *Ocean Waves Breaking and Marine Aerosol Fluxes* (Springer, New York, 2007).
[37] A. Babanin, *Breaking and Dissipation of Ocean Surface Waves* (Cambridge University Press, Cambridge, England, 2011).
[38] H. Lamb, *Hydrodynamics*, 6th ed. (Cambridge University Press, Cambridge, England, 1975).
[39] L. Shemer and S. K. Singh, Phys. Rev. Fluids **6**, 034802 (2021).